Journal of
Computational and Theoretical Nanoscience
Vol. 5, 201–213, 2008

Transmission Enhancement Through Nanoscale Metallic Slit Arrays from the Visible to Mid-Infrared

B. J. Lee, Y.-B. Chen, and Z. M. Zhang*

George W. Woodruff School of Mechanical Engineering, Georgia Institute of Technology, Atlanta, GA 30332, USA

In this paper, we systematically investigate the transmission enhancement through nanoscale metallic slit arrays in the wavelength range from visible to mid-infrared. The far-field transmittance of the periodic structure is calculated using the rigorous coupled-wave analysis (RCWA). The electromagnetic field distribution in the near-field regime is analyzed to elucidate three mechanisms for transmission enhancement. Depending on the spectral region, the enhanced transmission can be attributed to Wood's anomaly, cavity resonance, and the effective-medium behavior. The effects of grating/slit geometry, polarization, and the plane-of-incidence orientation on the radiation transmission are also examined.

Keywords: Electromagnetic Wave, Far-Field Transmittance, Nanoslits, Near-Field Effect.

RESEARCH ARTICLE

1. INTRODUCTION

Transmission enhancement through subwavelength hole arrays in an optically thick metal film has drawn much attention due to its potential in modulating the light path at nanometer scales.[1–3] The transmission through the periodic subwavelegnth apertures can overcome the diffraction limit of an individual aperture. In fact, when subwavelength apertures form a periodic two-dimensional (2D) array, the transmitted energy through an individual hole may be greater than the incident energy on the same area at certain wavelengths. Furthermore, plasmonic nanolithography has been demonstrated with 2D hole arrays.[4] The transmission enhancement through one-dimensional (1D) gratings or slit arrays has also been intensively studied, especially when the plane of incidence (PoI) is perpendicular to the grating grooves. The physical origin of the transmission enhancement can be attributed to one or more effect(s) of surface plasmon polariton (SPP) excitation,[5,6] cavity resonance,[7–9] and Wood's anomaly.[10,11]

It is well known that SPP can be excited in grating structures by propagating waves in air and the excitation results in enhanced absorption or transmission, especially for shallow gratings.[12,13] To excite SPP in gratings, a magnetic-field component parallel to the grating grooves is required.[14] A nonzero magnetic-field component exists in both the transverse magnetic (TM) and transverse electric (TE) waves, unless the PoI is either perpendicular or parallel to the grating grooves. When the PoI is perpendicular to grooves, only TM waves can excite SPPs; when the PoI is parallel to the grooves, only TE waves can excite SPPs. If the grating is sufficiently deep, cavity resonance caused by interference effects inside the 1D slits or 2D holes can also enhance the transmission.[9] In addition to the SPP excitation and cavity resonance, Wood's anomaly affects radiative properties and cause abrupt changes in the reflectance, transmittance, and absorptance spectra.[11] Wood's anomaly occurs when a diffraction order emerges or disappears at the grazing angle. The transmittance through a 1D slit array can be either enhanced or suppressed due to Wood's anomaly. Since Wood's anomaly occurs as a result of diffraction, both polarizations may exhibit such an anomaly. For shallow gratings when the PoI is perpendicular to the grooves, however, Wood's anomaly is not obvious for TE waves, and thus, initial studies only dealt with the anomaly for TM waves.[10]

Most of the previous studies dealt with transmission enhancement in the wavelength region from ultraviolet to near-infrared. For wavelengths much longer than the grating period, such as in the mid-infrared (IR), it is found that the transmission is large but cannot be attributed to any of the above mechanisms because the enhancement occurs in a wavelength-insensitive manner. Such transmission enhancement can be explained by the effective medium theory (EMT), in which the grating structure is viewed as a homogeneous medium if the wavelength is much longer than the grating period.[15] Based on rigorous electromagnetic wave modeling, we have previously shown a near-field localization effect of metallic slit arrays in the mid-IR region.[16]

*Author to whom correspondence should be addressed.

 1546-198X/2008/5/201/013 doi:10.1166/jctn.2008.008

The objective of the present study is to systematically investigate the far-field transmission enhancement from nanoscale metallic slit arrays in the wavelength regions from the visible to mid-IR with an emphasis on rigorous modeling. An effort is put to elucidate the transmission enhancement mechanisms by considering the electromagnetic field distribution in the vicinity of gratings, i.e., the near-field region. The transmittance of 1D periodic gratings is modeled based on the rigorous coupled-wave analysis (RCWA) algorithm. The enhanced transmission is explained by Wood's anomaly, cavity resonance, and effective medium behavior depending on the spectral region. The behavior of each mechanism is discussed in detail for nanoscale free-standing Ag gratings. Moreover, since the PoI is not necessarily perpendicular to the grooves, we have further examined the effect of non-zero azimuthal angle (i.e., conical diffraction). The RCWA formulation for conical diffraction is modified to improve the convergence efficiency.

2. RIGOROUS COUPLED-WAVE ANALYSIS FOR CONICAL DIFFRACTION

RCWA is a numerical modeling algorithm for calculating diffraction efficiencies of periodic gratings by solving Maxwell's equations. For 1D gratings, the RCWA algorithm is well established when the PoI is perpendicular to the grating grooves.[17] In this case, a modification to enhance the convergence efficiency has been proposed by Li for TM waves.[18] When the PoI is not perpendicular to the grating grooves, diffracted waves do not lie in the PoI except the zeroth order, and all the reflected waves lie on a conical surface (i.e., conical diffraction), whose center line is parallel to the grating grooves.[17] Similarly, all the transmitted waves also lie on the surface of another cone with a radius depending on the refractive index of the medium. Since most RCWA formulations for conical diffraction[17, 19, 20] were not modified according to Li's work,[18] the modified equations are summarized below.

Figure 1 shows a plane wave with wavevector $\mathbf{k}$ incident on a binary grating, where the space is divided into three regions: Region I (vacuum), Region II (grating), and Region III (substrate). The dielectric function (ε) of Regions I and III are given by $\varepsilon_{\mathrm{I}} = n_{\mathrm{I}}^2 = 1$, $\kappa_{\mathrm{I}} = 0$, and $\varepsilon_{\mathrm{III}} = (n_{\mathrm{III}} + i\kappa_{\mathrm{III}})^2$, where n is the refractive index and κ is the extinction coefficient. Since the grating region is composed of media A and B, its dielectric function, composed of ε_{A} and ε_{B}, is a periodic function of x. The geometry of gratings is defined by the period (Λ), thickness (d), and the slit width (w). The filling ratio of medium A is given by $f = 1 - w/\Lambda$. The direction of incident wave is expressed by the azimuthal angle (ϕ) and the zenith angle (θ). The PoI is conventionally defined by the direction of incidence and the z axis. This definition results in infinite numbers of PoI at normal incidence. To remedy this drawback, we

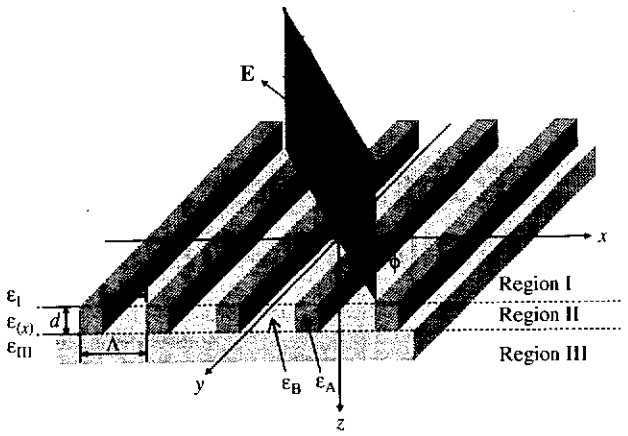

Fig. 1. Schematic of a binary 1D grating, whose geometry is defined by the period (Λ), thickness (d), and slit width (w). The direction of the incident plane wave is defined by the zenith angle θ and the azimuthal angle ϕ, and ψ represents the angle between the oscillation direction of electric field and the plane of incidence.

can uniquely define the PoI by the z axis and the vector $(\cos\phi, \sin\phi, 0)$, which lies in the x–y plane. In practice, it is convenient to define the PoI for normal incidence by setting $\sin\phi = 0$. This way, the PoI is perpendicular to the grooves. For linearly polarized incident wave, the polarization status is determined by ψ, which is the angle between the electric field vector and the PoI, as shown in Figure 1. In Region I, after omitting the time harmonic term $\exp(-i\omega t)$, where ω is the angular frequency, the normalized incident electric-field vector $\mathbf{E}$ is given by

$$\mathbf{E} = \mathbf{E}_i \exp\left(ik_x x + ik_y y + ik_z z\right) \tag{1}$$

where $\mathbf{E}_i$ is the incident electric field vector at the origin, and the components of the incident wavevector are given by $k_x = k\sin\theta\cos\phi$, $k_y = k\sin\theta\sin\phi$, and $k_z = k\cos\theta$, with $k = 2\pi/\lambda$. In the present study, λ denotes the vacuum wavelength. The incident electric field can be normalized so that the unit vector $\mathbf{E}_i$ is expressed as follows:

$$\begin{aligned}\mathbf{E}_i = {} & (\cos\psi\cos\theta\cos\phi - \sin\psi\sin\phi)\hat{\mathbf{x}} \\ & + (\cos\psi\cos\theta\sin\phi + \sin\psi\cos\phi)\hat{\mathbf{y}} \\ & - \cos\psi\sin\theta\hat{\mathbf{z}}\end{aligned} \tag{2}$$

According to the Bloch-Floquet condition,[21] the wavevector components of the jth diffraction order in Region I are given by

$$k_{xj} = \frac{2\pi}{\lambda}\sin\theta\cos\phi + \frac{2\pi}{\Lambda}j \tag{3a}$$

$$k_y = \frac{2\pi}{\lambda}\sin\theta\sin\phi \tag{3b}$$

$$k_{zj}^r = \begin{cases} \sqrt{k^2 - k_{xj}^2 - k_y^2}, & k^2 > k_{xj}^2 + k_y^2 \\ i\sqrt{k_{xj}^2 + k_y^2 - k^2}, & k_{xj}^2 + k_y^2 > k^2 \end{cases} \tag{3c}$$

As required by the phase-matching condition, the parallel components of wavevector k_{xj} and k_y must be the same for the diffracted waves in all three regions. In Eq. (3c), superscript r refers to the reflected diffraction. We may denote the reflected wavevectors by $\mathbf{k}_{rj} = (k_{xj}, k_y, k^r_{zj})$ and the transmitted wavevectors by $\mathbf{k}_{tj} = (k_{xj}, k_y, k^t_{zj})$. For transmitted diffraction, k^r_{zj} can be replaced by k^t_{zj} after substituting $k_{III} = k\sqrt{\varepsilon_{III}}$ for k in Eq. (3c). Figure 2 shows the wavevectors of the incident wave and diffracted waves in 3D k-space and their projections on the k_x–k_z plane. Notice that the wavevector magnitude for incident and refracted waves (medium 1) is k. The wavevector magnitude for the transmitted waves is k_{III}, which is assumed to be greater than k. From Eq. (3b), the y component of the wavevector is the same for all diffraction orders. Hence, the wavevectors for all the diffracted wavevectors end on the semi-circles, which are intersects of the plane $k_y = (2\pi/\lambda)\sin\theta\sin\phi$ and hemispherical surfaces in each half plane. Talking $k_z < 0$ or Region I for example, all the reflected waves lie on a half-conical surface, as illustrated in Figure 2(a) for conical diffraction. Furthermore,

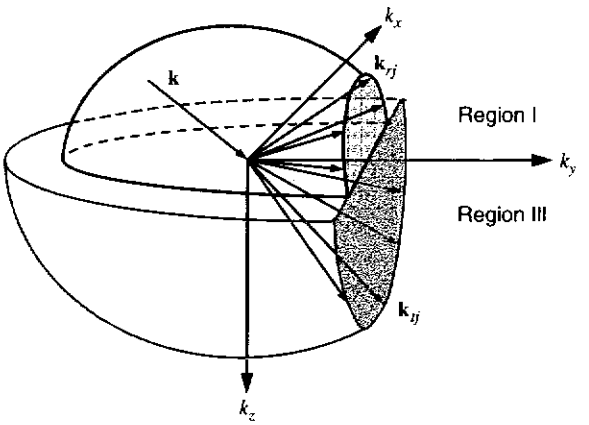

(a) 3D k-space

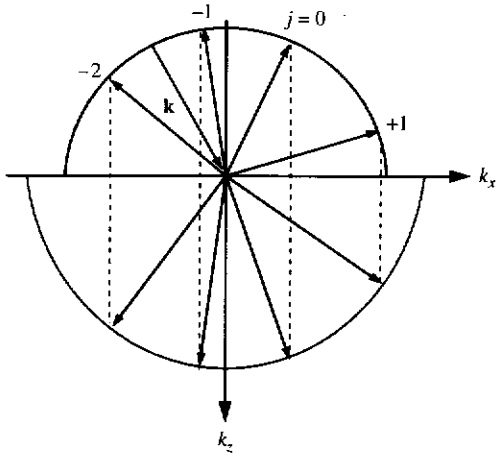

(b) Projected to k_x–k_z plane

Fig. 2. Illustrations of a conical diffraction from a 1D grating in: (a) 3D k-space; (b) projected to k_x–k_z plane.

the x components of the wavevectors vary by multiples of $2\pi/\Lambda$ according to Eq. (3a). The dashed vertical lines in Figure 2(b) indicate $2\pi/\Lambda$ difference in k_x among adjacent diffraction orders. For higher diffraction orders, the z component of the wavevector becomes purely imaginary, such that the diffracted waves are evanescent. If the PoI is perpendicular to the gratings, $\phi = 0°$ or 180°, then, both $\sin\phi$ and k_y become zero; subsequently, all the reflected and transmitted diffraction rays lie in the same plane as the PoI.

Sufficient diffraction orders must be employed in the RCWA calculation such that $j = 0, \pm1, \pm2, \ldots, \pm q$, with a total of $N = 2q+1$ terms. The electric field in Regions I and III can be expressed as

$$\mathbf{E}_I(x,y,z) = \mathbf{E}_i \exp(ik_x x + ik_y y + ik_z z) + \sum_j \mathbf{E}_{rj} \exp(ik_{xj}x + ik_y y - ik^r_{zj} z) \quad (4a)$$

and

$$\mathbf{E}_{III}(x,y,z) = \sum_j \mathbf{E}_{tj} \exp(ik_{xj}x + ik_y y + ik^t_{zj} z) \quad (4b)$$

where $\mathbf{E}_{rj} = (E^r_{xj}, E^r_{yj}, E^r_{zj})$ and $\mathbf{E}_{tj} = (E^t_{xj}, E^t_{yj}, E^t_{zj})$. The magnetic fields in Regions I and III can be obtained from Maxwell's equation, $\mathbf{H} = (1/i\omega\mu_0)\nabla \times \mathbf{E}$ where μ_0 is the magnetic permeability of vacuum. In Region II, the electric and magnetic fields can be expressed as a Fourier series:

$$\mathbf{E}_{II}(x,y,z) = \sum_j [\chi_{xj}(z)\hat{\mathbf{x}} + \chi_{yj}(z)\hat{\mathbf{y}} + \chi_{zj}(z)\hat{\mathbf{z}}] \exp(ik_{xj}x + ik_y y) \quad (5a)$$

$$\mathbf{H}_{II}(x,y,z) = i\frac{k}{\mu_0\omega} \sum_j [\gamma_{xj}(z)\hat{\mathbf{x}} + \gamma_{yj}(z)\hat{\mathbf{y}} + \gamma_{zj}(z)\hat{\mathbf{z}}] \exp(ik_{xj}x + ik_y y) \quad (5b)$$

where χ_{xj}, χ_{yj}, and χ_{zj} are the vector components for the jth space-harmonic electric field, and γ_{xj}, γ_{yj}, and γ_{zj} are the vector components for the jth space-harmonic magnetic field in the grating region. Due to the periodicity, the dielectric function in Region II can also be expressed in a Fourier expansion

$$\varepsilon^{ord}(x) = \varepsilon(x) = \sum_p \varepsilon^{ord}_p \exp\left(i\frac{2p\pi}{\Lambda}x\right) \quad (6a)$$

It is essential to express the inverse of the dielectric function in Region II as a separate Fourier expansion, i.e.,

$$\varepsilon^{inv}(x) = \frac{1}{\varepsilon(x)} = \sum_p \varepsilon^{inv}_p \exp\left(i\frac{2p\pi}{\Lambda}x\right) \quad (6b)$$

where ε^{ord}_p and ε^{inv}_p are the pth Fourier coefficient for the ordinary and inverse of $\varepsilon(x)$ as defined in Eqs. (6a)

and (6b), respectively; and in general, $\varepsilon_p^{\text{inv}} \neq 1/\varepsilon_p^{\text{ord}}$. In the numerical calculation, an upper limit of p can be set such that $p = 0, \pm 1, \pm 2, \ldots, \pm 2q$, which means that there are a total of $2q+1$ terms in the Fourier series. The choice between Eqs. (6a) or (6b) is crucial to the modified RCWA formulation.

The next step is to substitute the electric and magnetic fields given in Eqs. (5a) and (5b), respectively, into Maxwell's equations in Region II: $\nabla \times \mathbf{E}_{\text{II}} - i\omega\mu_0 \mathbf{H}_{\text{II}} = 0$ and $\nabla \times \mathbf{H}_{\text{II}} + i\omega\varepsilon_0 \varepsilon(x)\mathbf{E}_{\text{II}} = 0$, where ε_0 is the electric permittivity of vacuum. The key is to arrange Maxwell's equations into a summation of $\exp(ik_{xj}x + ik_y y)$ and then set its coefficients to zero for each j. However, one must be very cautious when factorizing $\exp(ik_{xj}x + ik_y y)$, because both $\varepsilon^{\text{ord}}(x)$ and $\varepsilon^{\text{inv}}(x)$ are Fourier expansions of $\exp(ik_{xj}x)$. The mathematical rules discussed in the work of Li[18] must be properly applied. Failure of doing so can result in slow convergence and even erroneous solutions. After collecting all the terms, four sets of coupled differential equations can be obtained for the tangential components of the electric and magnetic fields: χ_{xj}, χ_{yj}, γ_{xj}, and γ_{yj} since the normal components χ_{zj} and γ_{zj} can be related to the tangential components. After some tedious derivations, the differential equations can be expressed in the matrix form:

$$\frac{1}{k}\begin{bmatrix} \partial \mathbf{X}^Y/\partial z \\ \partial \mathbf{X}^X/\partial z \\ \partial \mathbf{\Gamma}^Y/\partial z \\ \partial \mathbf{\Gamma}^X/\partial z \end{bmatrix} = \begin{bmatrix} \mathbf{0} & \mathbf{0} & \mathbf{K}^Y\mathbf{E}^{-1}\mathbf{K}^X & \mathbf{I}-\mathbf{K}^Y\mathbf{E}^{-1}\mathbf{K}^Y \\ \mathbf{0} & \mathbf{0} & \mathbf{K}^X\mathbf{E}^{-1}\mathbf{K}^X-\mathbf{I} & -\mathbf{K}^X\mathbf{E}^{-1}\mathbf{K}^Y \\ \mathbf{K}^X\mathbf{K}^Y & \mathbf{M}^{-1}-\mathbf{K}^Y\mathbf{K}^Y & \mathbf{0} & \mathbf{0} \\ \mathbf{K}^X\mathbf{K}^X-\mathbf{E} & -\mathbf{K}^X\mathbf{K}^Y & \mathbf{0} & \mathbf{0} \end{bmatrix} \begin{bmatrix} \mathbf{X}^Y \\ \mathbf{X}^X \\ \mathbf{\Gamma}^Y \\ \mathbf{\Gamma}^X \end{bmatrix} \tag{7}$$

where $\mathbf{X}^X$ and $\mathbf{X}^Y$ are column vectors formed by χ_{xj} and χ_{yj}, respectively, $\mathbf{\Gamma}^X$ and $\mathbf{\Gamma}^Y$ are column vectors formed by γ_{xj} and γ_{yj}, and $\mathbf{I}$ is the unit matrix. Note that $\mathbf{K}^X$ and $\mathbf{K}^Y$ are diagonal matrices with the elements $K^X_{l,l} = k_{xj}/k$, where $j = l-q-1$ and $K^Y_{l,l} = k_y/k$. Furthermore, $\mathbf{E}$ and $\mathbf{M}$ are the Toeplitz matrices[18] generated by the Fourier coefficients of the dielectric function and its inverse, respectively, such that $E_{l,m} = \varepsilon_p^{\text{ord}}$ and $M_{l,m} = \varepsilon_p^{\text{inv}}$, where $p = l-m$. Equation (7) shows the modified matrix form for conical diffraction, which is different mathematically from Refs. [17] and [20], because the selection between matrices $\mathbf{E}$ and $\mathbf{M}$ here is in accordance with Li's recommended procedure. In order to solve Eq. (7), $\mathbf{X}^X$ and $\mathbf{X}^Y$ can be decoupled from $\mathbf{\Gamma}^X$ and $\mathbf{\Gamma}^Y$ by differentiating another time. In a similar way, $\mathbf{\Gamma}^X$ and $\mathbf{\Gamma}^Y$ can be decoupled from $\mathbf{X}^X$ and $\mathbf{X}^Y$. Note that matrix equation in Ref. [22] is consistent with Eq. (7); however, the authors did differently in the second derivations. The proper matrix equations for $\mathbf{X}$ and $\mathbf{\Gamma}$ are as follows:

$$\frac{1}{k^2}\begin{bmatrix} \dfrac{\partial^2 \mathbf{X}^Y}{\partial z^2} \\ \dfrac{\partial^2 \mathbf{X}^X}{\partial z^2} \end{bmatrix} = \begin{bmatrix} \mathbf{K}^X\mathbf{K}^X & \mathbf{K}^Y(\mathbf{E}^{-1}\mathbf{K}^X\mathbf{E}-\mathbf{K}^X) \\ \mathbf{0} & \mathbf{K}^Y\mathbf{K}^Y+(\mathbf{K}^X\mathbf{E}^{-1}\mathbf{K}^X-\mathbf{I})\mathbf{M}^{-1} \end{bmatrix} \begin{bmatrix} \mathbf{X}^Y \\ \mathbf{X}^X \end{bmatrix} \tag{8a}$$

$$\frac{1}{k^2}\begin{bmatrix} \dfrac{\partial^2 \mathbf{\Gamma}^Y}{\partial z^2} \\ \dfrac{\partial^2 \mathbf{\Gamma}^X}{\partial z^2} \end{bmatrix} = \begin{bmatrix} \mathbf{K}^Y\mathbf{K}^Y+\mathbf{M}^{-1}(\mathbf{K}^X\mathbf{E}^{-1}\mathbf{K}^X-\mathbf{I}) & (\mathbf{K}^X-\mathbf{M}^{-1}\mathbf{K}^X\mathbf{E}^{-1})\mathbf{K}^Y \\ \mathbf{0} & \mathbf{K}^X\mathbf{K}^X+\mathbf{E}(\mathbf{K}^Y\mathbf{E}^{-1}\mathbf{K}^Y-\mathbf{I}) \end{bmatrix} \begin{bmatrix} \mathbf{\Gamma}^Y \\ \mathbf{\Gamma}^X \end{bmatrix} \tag{8b}$$

Accordingly, the solutions of χ_{xj}, χ_{yj}, γ_{xj}, and γ_{yj} can be expressed by the eigenvalue and eigenvectors of the matrices given by

$$\chi_{xj}(z) = \sum_{l=1}^{N} W^A_{j,l}[C_l^{A+}e^{k\xi_l(z-d)} + C_l^{A-}e^{-k\xi_l z}] \tag{9a}$$

$$\gamma_{xj}(z) = \sum_{l=1}^{N} W^B_{j,l}[C_l^{B+}e^{k\zeta_l(z-d)} + C_l^{B-}e^{-k\zeta_l z}] \tag{9b}$$

$$\chi_{yj}(z) = \sum_{l=1}^{N} V^{AA}_{j,l}[C_l^{A+}e^{k\xi_l(z-d)} + C_l^{A-}e^{-k\xi_l z}] + \sum_{l=1}^{N} V^{AB}_{j,l}[C_l^{B+}e^{k\zeta_l(z-d)} - C_l^{B-}e^{-k\zeta_l z}] \tag{9c}$$

$$\gamma_{yj}(z) = \sum_{l=1}^{N} V^{BA}_{j,l}[C_l^{A+}e^{k\xi_l(z-d)} - C_l^{A-}e^{-k\xi_l z}] + \sum_{l=1}^{N} V^{BB}_{j,l}[C_l^{B+}e^{k\zeta_l(z-d)} + C_l^{B-}e^{-k\zeta_l z}] \tag{9d}$$

where $W^A_{j,l}$ and $W^B_{j,l}$ are the elements of the matrices $\mathbf{W}^A$ and $\mathbf{W}^B$, and they are composed of the eigenvector corresponding to the eigenvalue of the matrices

$$\mathbf{A} = \mathbf{K}^Y\mathbf{K}^Y + (\mathbf{K}^X\mathbf{E}^{-1}\mathbf{K}^X - \mathbf{I})\mathbf{M}^{-1} \tag{10a}$$

and

$$\mathbf{B} = \mathbf{K}^X\mathbf{K}^X + \mathbf{E}(\mathbf{K}^Y\mathbf{E}^{-1}\mathbf{K}^Y - \mathbf{I}) \tag{10b}$$

The exponential terms in Eqs. (9a) and (9b) originate from the forward and backward coupled diffracted waves in Region II. Here, C's are their unknown coefficients with superscripts + and − which signify forward and backward waves. Note that ξ_l and ζ_l are the elements of diagonal matrices $\mathbf{Q}^A$ and $\mathbf{Q}^B$, which are composed of the positive square root of the eigenvalue of $\mathbf{A}$ and $\mathbf{B}$. In addition, $V^{AA}_{j,l}$,

$V_{j,l}^{AB}$, $V_{j,l}^{BA}$, and $V_{j,l}^{BB}$ are the elements of matrices $\mathbf{V}^{AA}$, $\mathbf{V}^{AB}$, $\mathbf{V}^{BA}$, and $\mathbf{V}^{BB}$, respectively, given by

$$\mathbf{V}^{AA} = \mathbf{K}^{Y}(\mathbf{K}^{X}\mathbf{K}^{X} - \mathbf{E})^{-1}\mathbf{K}^{X}\mathbf{W}^{A} \quad (11a)$$

$$\mathbf{V}^{AB} = (\mathbf{K}^{X}\mathbf{K}^{X} - \mathbf{E})^{-1}\mathbf{W}^{B}\mathbf{Q}^{B} \quad (11b)$$

$$\mathbf{V}^{BA} = (\mathbf{K}^{X}\mathbf{E}^{-1}\mathbf{K}^{X} - \mathbf{I})^{-1}\mathbf{W}^{A}\mathbf{Q}^{A} \quad (11c)$$

and

$$\mathbf{V}^{BB} = \mathbf{K}^{Y}(\mathbf{K}^{X}\mathbf{E}^{-1}\mathbf{K}^{X} - \mathbf{I})^{-1}\mathbf{K}^{X}\mathbf{E}^{-1}\mathbf{W}^{B} \quad (11d)$$

In order to obtain complete field distributions in Regions I, II, and III, one needs to solve for $10N$ unknown coefficients, i.e., E_{xj}^{r}, E_{yj}^{r}, E_{zj}^{r}, E_{xj}^{t}, E_{yj}^{t}, E_{zj}^{t}, C_{j}^{A+}, C_{j}^{A-}, C_{j}^{B+}, and $C_{j}^{B-}(j = 1, 2, \ldots, N)$. Here, boundary conditions state that the tangential components of the electric and magnetic fields are continuous at region boundaries ($z = 0$ and $z = d$). Application of the boundary conditions yields $8N$ equations. Furthermore, since diffracted waves are assumed to be plane waves, they should be perpendicular to the corresponding wavevector; therefore,

$$\mathbf{k}_{rj} \cdot \mathbf{E}_{rj} = 0 \quad (12a)$$

and

$$\mathbf{k}_{tj} \cdot \mathbf{E}_{tj} = 0 \quad (12b)$$

which provide additional $2N$ equations. After solving the $10N$ coefficients, one can get the diffraction efficiencies by computing the time-averaged Poynting vector of each diffraction order along the z direction. Furthermore, the field distribution and Poynting vector distribution in the near field are completely obtained. Notice that RCWA can, in principle, achieve accuracy to an arbitrarily specified degree by the use of sufficient numbers of Fourier components to represent the dielectric function in the grating region. In the present study, a total of 81 Fourier terms (i.e., $N = 81$) are used and the results differ from those obtained with 201 terms by less than 0.3%. For a given wavelength and geometric parameters, the calculation of the transmittance using RCWA algorithm takes about 0.5 s of CPU time with a Pentium 4 processor (3.2 GHz speed).

3. RESULTS AND DISCUSSION

In the present study, a vacuum is assumed for the media below and above the gratings as well as the slit region for simplicity. The transmission enhancement is demonstrated by selecting silver (Ag) as the metal. It should be noted that for practical applications, a dielectric substrate can be used to support the metallic grating structure, and the discussion presented here will still be applicable. The nanoscale metallic grating can be fabricated by lithography (deep UV, X-ray, or electron beam), nano-imprinting, or focused ion beam machining. Metals can be evaporated onto the space patterned by the photoresist and the desired structures remain after stripping the photoresist. Besides silver, gold and aluminum can be used for a metallic grating with very similar transmission characteristics in the infrared.

Figures 3(a and b) show the spectral transmittance for a free-standing Ag grating at normal incidence. The grating geometric parameters are set such that $\Lambda = 400$ nm, $d = 800$ nm, and $w = 200$ nm (i.e., the Ag filling ratio $f = 0.5$). The azimuthal angle ϕ is set to 0° so that the PoI is perpendicular to the grating grooves. The transmittance is plotted against the wavelength from 0.3 to 9.0 μm for both the TE wave ($\psi = 90°$) and the TM wave ($\psi = 0°$). The tabulated optical constants of Ag in Ref. [23] are used with interpolation. An 800-nm-thick Ag film is essentially opaque in the wavelength region considered, because the radiation penetration depth is less than 50 nm; however, a large transmittance is observed from the Ag slit array at certain wavelengths for both TE and TM waves. For the TE wave as shown in Figure 3(a),

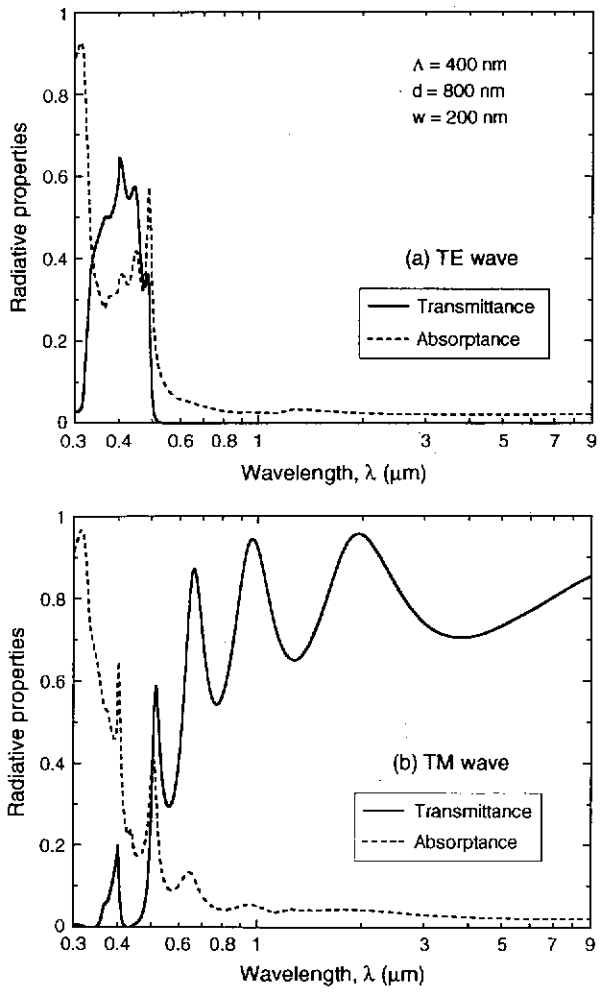

Fig. 3. Transmittance and absorptance of the free-standing Ag grating with $\Lambda = 400$ nm, $d = 800$ nm, and $w = 200$ nm when the plane of incidence is perpendicular to the grating grooves for: (a) TE wave; (b) TM wave.

the large transmittance is obtained in the spectral band from 300 to 500 nm. This is due to Wood's anomaly ($\lambda = \Lambda = 400$ nm) and cavity resonance, such that the transmittance peaks are closely located and partly overlap each other. The transmittance in the IR region is close to zero with the absorptance value less than 0.05; thus, most of the incident energy is reflected back by the Ag grating. On the contrary, the spectral transmittance for the TM wave as shown in Figure 3(b) exhibits strong enhancement over the wavelength range from the visible to the mid-IR spectral region. Wood's anomaly and cavity resonance result in considerable transmission enhancement, especially at wavelengths less than 2 μm. However, more cavity resonance peaks are observed for TM waves and their transmittance values are greater than those for TE waves. Furthermore, the peak wavelengths from the cavity resonance shift to the longer wavelength region for TM waves. Interestingly, when the wavelength is greater than 4 μm, the transmittance for TM waves increases monotonically and reaches 0.85 at $\lambda = 9$ μm, suggesting that enhancement is not due to resonance phenomena. The large transmittance enhancement in the mid-IR for TM waves can be explained by the effective medium behavior when $\lambda \gg \Lambda$ and will be discussed in detail later.

It should be noted that for the considered Ag slit array, SPP plays an insignificant role in terms of the transmission enhancement. Because the thickness of grating is much greater than the radiation penetration depth, SPPs at two region boundaries (i.e., $z = 0$ and $z = d$) are decoupled. In this case, SPP can only be excited at one boundary since the diffracted evanescent wave cannot reach the other boundary. Accordingly, the excitation of SPP at $z = 0$ mainly contributes to absorption rather than transmission. Here, SPP occurs at the wavelength very close to that of Wood's anomaly, because the dispersion curve is close to the light line in vacuum.[24] Consequently, the transmittance at 400 nm for TM waves is less than that for TE waves due to the absorption accompanied with the excitation of SPP, as can be seen from Figure 3(b). Therefore, the effect of SPP on the transmission enhancement is not further considered in the present study. Detail discussions about Wood's anomaly, cavity resonance, and the effective medium behavior and their role in modulating the radiative properties are provided below.

3.1. Wood's Anomaly

Wood's anomaly occurs when a diffraction order shows up at the grazing angle. The radiative properties abruptly change at the wavelength corresponding to Wood's anomaly because the light intensity will be redistributed when a new propagating diffraction order appears. Originally, Wood's anomaly was studied for grating structures on a semi-infinite substrate, such that its effects were prominent in the reflectance spectrum,[11] and a few studies dealt with Wood's anomaly on the transmittance.[25,26] In this case, the anomalies in both Regions I and III may affect the spectral transmittance of periodic slit arrays.

For conical diffraction, the jth diffraction order appears at the grazing angle (when the z component of the wavevector becomes zero) in Regions I and III when $k_{xj}^2 + k_y^2 = k^2$ because both regions are set to be vacuum. Using Eqs. (3a) and (3b), Wood's anomaly can be predicted from the following equation for an arbitrary ψ:

$$\left(\frac{\lambda}{\Lambda} j\right)^2 + 2\frac{\lambda}{\Lambda} j \sin\theta\cos\phi - \cos^2\theta = 0 \qquad (13)$$

Since Wood's anomaly occurs due to diffraction, it is obvious that Eq. (13) only depends on the grating period regardless of its thickness and filling ratio. Equation (13) can be further simplified if the PoI is perpendicular to the grating grooves (i.e., $\phi = 0°$).[21] In this case, ± 1 diffraction orders appear when the wavelength is equal to the grating period at normal incidence as shown in Figures 3(a) and (b) when $\lambda = 400$ nm. Since the considered Ag grating is relatively deep (i.e., $\Lambda/d = 0.5$), Wood's anomaly can

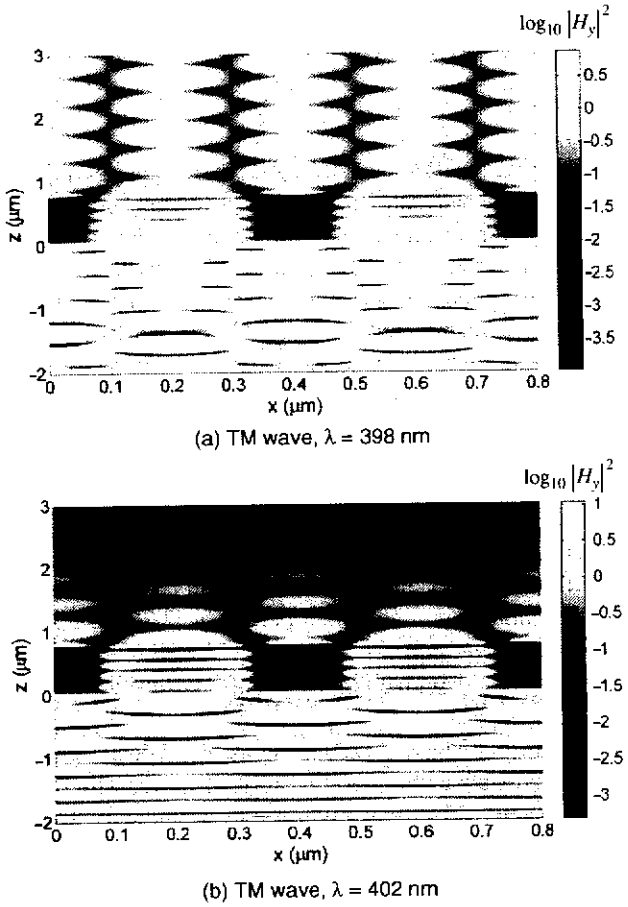

Fig. 4. Square of the magnitude of complex magnetic field in logarithmic scale for TM wave over the two grating periods: (a) $\lambda = 398$ nm; (b) $\lambda = 402$ nm. The geometric parameters of the Ag grating are the same as in Figure 3, and the slit regions are located in 0.1 μm $\le x \le$ 0.3 μm as well as 0.5 μm $\le x \le$ 0.7 μm. The wave is incident from below the slit array.

be clearly seen for both TE and TM waves. If the grating is relatively shallow, the effects of Wood's anomaly on radiative properties may not be obvious for TE waves as compared to TM waves.[21] In order to further understand the characteristics of Wood's anomaly, the square of the magnitude of complex magnetic field is plotted in logarithmic scale (i.e., $\log_{10}|H_y|^2$) for TM waves at two wavelengths very close to that associated with Wood's anomaly. For TE waves, a very similar field distribution will be obtained if the electric field is plotted.

Figures 4(a) and (b) show the magnetic field distribution over two grating periods at $\lambda = 398$ nm ($T = 0.180$) and $\lambda = 402$ nm ($T = 0.141$), respectively, in the vicinity of the Ag grating. The grating geometry is the same as that in Figure 3. The slit regions are located in $0.1\ \mu\text{m} \le x \le 0.3\ \mu\text{m}$ as well as $0.5\ \mu\text{m} \le x \le 0.7\ \mu\text{m}$, and a plane wave is incident from the below the grating at normal incidence. Wood's anomaly occurs at $\lambda = 400$ nm and the transmittance is 0.199. In Figure 4(a), the wavelength of 398 nm is a little shorter than the grating period such that the diffraction orders of $j = \pm 1$ propagate to the far field. Since there exists no energy loss in vacuum, the field distribution in Region I (below the grating in Fig. 4(a)) shows very similar patterns in the near field as well as in the far field. In fact, the periodic interference patterns are found in the field distribution in both x and z directions. Here, the periodic pattern of the field along the x direction results from the $j = \pm 1$ diffracted waves, which are propagating nearly along the region boundary (i.e., $k_{xj} \approx k$). Since the plane wave has an infinite wave front, the periodic interference patterns in the x direction are observed even if z approaches negative infinity from the grating surface. On the other hand, the periodic pattern along the negative z direction is due to the interferences among diffracted waves, whose orders are 0 and ± 1, as well as the incident wave. The transmitted waves in Region III show very similar interference patterns as in Region I. Notice that when Wood's anomaly occurs (i.e., $k_{xj} = k$ for $j = \pm 1$), the field distribution should be very similar to Figure 4(a).

On the contrary, at the wavelength of 402 nm, the ± 1 diffraction orders are evanescent waves. As can be seen from Figure 4(b), when the distance from the surface is less than 1.5 μm, the interference patterns in Region I are very similar to those in Figure 4(a), with periodicity in both x and z directions. However, the periodic interference pattern in the x direction is due to evanescent waves along the boundary. Since the imaginary part of the z component of the wavevector is very small for $j = \pm 1$ diffracted waves, the periodic patterns in the x direction appear even when $|z|/\lambda \approx 4$. If the distance from the surface further increases, only interference patterns in the z direction remain. In fact, the magnetic field of Region I is greatly affected by evanescent waves in the near field regime and is quite different from that in the far field, where evanescent waves disappear. The magnetic field pattern in the far field is the interference of the zeroth-order diffracted wave and the incident wave. Likewise, the transmitted fields show very similar distributions as in Region I. Consequently, the field distribution in the near-field and far-field regimes clearly indicates that $j = \pm 1$ propagating orders disappear at a wavelength slightly longer than that corresponding to Wood's anomaly. In addition, the near-field distribution reveals very rich features due to the interference between evanescent waves and propagating waves. It should be noted that Wood's anomaly may not always enhance the transmission, and other studies showed that the transmittance could be suppressed.[25] The effects of Wood's anomaly on the transmittance also depend on the angle of incidence according to Eq. (13).

3.2. Cavity Resonance

When the cavity resonance occurs, standing waves exist in cavities formed by the grating. At the resonance condition, a strong electromagnetic field exists inside the cavity or slit; it is the confined and enhanced field that subsequently enhances transmission through the gratings. Therefore, several peaks can be observed from the far-field transmittance spectra as shown in Figure 3. Notice that each cavity formed by the grating has two open ends at $z = 0$ and $z = d$. However, the boundary condition requires that tangential field components be continuous, enabling electromagnetic waves to be confined inside the cavity. Consequently, the resonance condition strongly depends on the geometric parameters of the cavity as well as the boundary conditions. Furthermore, the boundary conditions are complicated functions of geometric parameters. The cavity resonance is not the same as an 1D Fabry-Pérot resonance, whose resonance condition is simply given by $n_c d_c$ = multiples of $\lambda/2$, where n_c and d_c are respectively the refractive index and thickness of the medium inside the 1D cavity.[27] Therefore, the resonance condition suggested by Refs. [28] and [29] does not properly predict the cavity resonance condition of the gratings studied here. In fact, the standing wave in the cavity is a combination of all diffracted waves including evanescent waves, and it is not necessary for a single diffraction component to contribute to the cavity resonance. As Lezec and Thio[3] pointed out for 2D hole arrays, interferences of diffracted evanescent waves must be fully considered to predict the transmittance peak position. To further understand the cavity resonance of 1D gratings, the field distribution is plotted in the near-field regime and discussed next.

At selected peak wavelengths, the squares of magnetic and electric fields are plotted for TM and TE waves, respectively, over two grating periods in Figure 5. The grating geometry is the same as that in Figure 3. Figure 5(a) plots the magnetic field distribution for TM waves when the wavelength is 1950 nm at which the transmittance $T = 0.957$. The slit regions are for $0.1\ \mu\text{m} \le x \le 0.3\ \mu\text{m}$ and $0.5\ \mu\text{m} \le x \le 0.7\ \mu\text{m}$, and the wave is incident from the bottom of the grating at normal incidence.

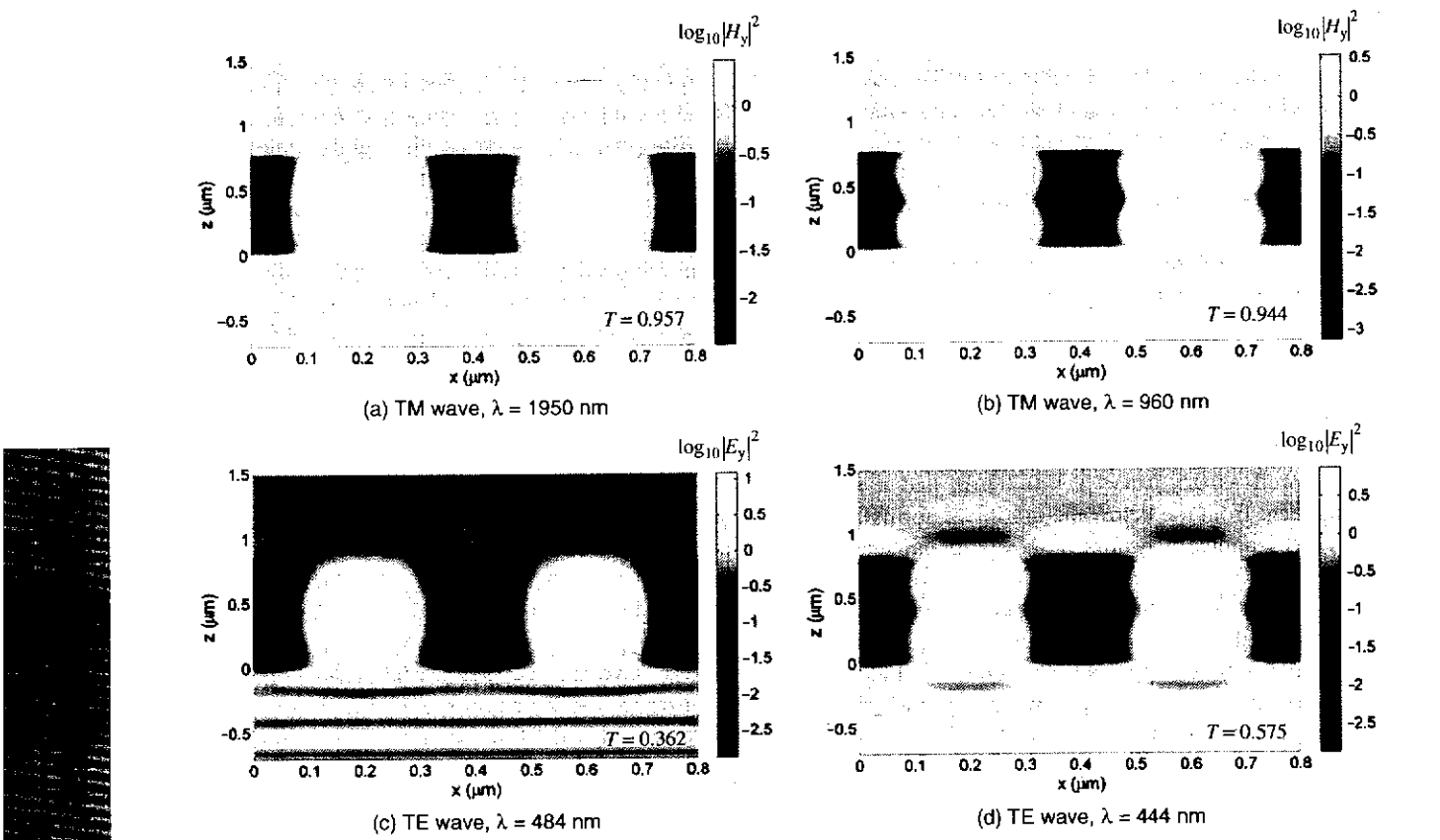

Fig. 5. Square of the magnitude of complex magnetic field when the cavity resonance occurs for TM waves over the two grating periods: (a) λ = 1950 nm; (b) $\lambda = 960$ nm and that of complex electric field for TE waves: (c) $\lambda = 484$ nm; (d) $\lambda = 444$ nm. The geometric parameters of the Ag grating are the same as in Figures 3 and 4. The corresponding transmittance T is also indicated for each case.

The magnetic field distribution clearly indicates that one anti-node (i.e., maximum of the field intensity) is formed at the center of the cavity. As the wavelength further increases, no cavity mode exists, and thus, the transmittance does not show such peaks. This suggests that the wavelength of 1950 nm corresponds to the cutoff wavelength (upper limit) of the cavity resonance. When the wavelength decreases to 960 nm where the transmittance $T = 0.944$, two anti-nodes are formed in the cavity as illustrated in Figure 5(b). Note again that because of the complex coupling of diffracted waves, the wavelength at which two anti-nodes occur slightly vary from half of the wavelength at which a single anti-node occurs. Even though it is not shown, if the magnetic field is plotted at 1260 nm, where the transmittance dip exists, one-and-a-half anti-nodes are formed in the cavity region. Accordingly, multiple anti-nodes will be found inside the cavity when the wavelength further decreases, corresponding to higher modes (or overtones) of the cavity resonance. However, only low-order cavity resonance modes contribute to the high transmittance peaks, and the transmittance for high-order modes may not necessarily show a high peak.

For TE waves, very similar field distributions are obtained when the transmittance shows peaks as illustrated in Figures 5(c and d). The cutoff wavelength for the TE wave occurs at 484 nm, which is about one-quarter of the cutoff wavelength for the TM wave. In fact, there are four anti-nodes at 514 nm in the TM wave due to cavity resonance, which is not shown in Figure 5. Interestingly, the wavelength associated with two anti-nodes for the TE wave occurs at 444 nm; this is very close to the cutoff wavelength of 484 nm, suggesting that the frequency at which two anti-nodes occur is far from twice the frequency at which only one anti-node occurs. In addition, the grating becomes almost opaque for TE wave when the wavelength is longer than 500 nm. It can be seen from Figures 5(a and b) that, while cavity resonance can enhance the transmittance for both polarizations, the peak locations and the number of anti-nodes are polarization dependent. The enhancement of transmittance for TE waves by cavity resonance is not as significant as in the case of TM waves. In the following, the effects of geometric parameters, such as the grating thickness, period, and slit width on the resonance condition are separately investigated only for TM waves.

Figure 6(a) shows the transmittance spectra when Λ = 400 nm and $w = 200$ nm are fixed for $d = 400$ nm, 800 nm, and 1600 nm. As the grating thickness increases, more transmittance peaks are found in the considered wavelength range; and furthermore, the cutoff wavelength shifts to the

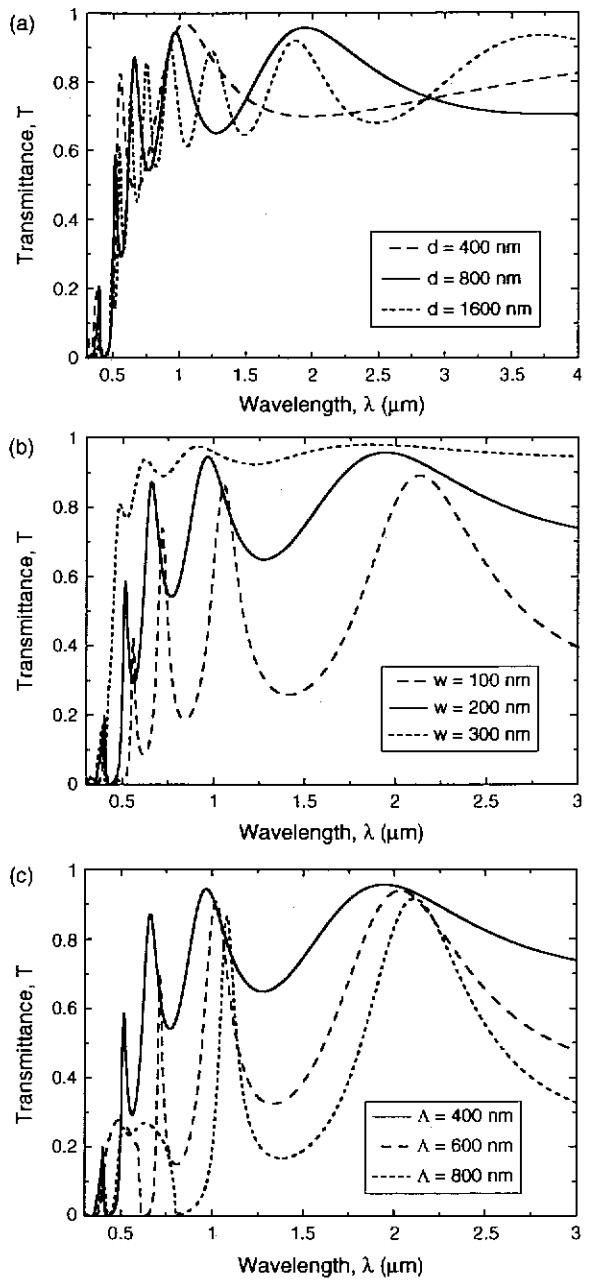

Fig. 6. Effects of the geometric parameters on the cavity resonance of Ag gratings for TM wave. The geometric parameters of the base case are $\Lambda = 400$ nm, $d = 800$ nm, $w = 200$ nm, and $\phi = 0°$. Only one of the parameters is varied in each of the following cases: (a) different thicknesses; (b) different slit widths; (c) different periods.

longer wavelength region. This is related to the standing wave formation with one anti-node similar to what is seen in Figure 5(a). The wavelength of the standing wave with one anti-node should be longer when the cavity thickness increases. Though the thickness changes by factor of two, no transmittance peak occurs at the same wavelength for three cases. This supports that the cavity resonance is much more complicated than for a simple Fabry-Pérot resonance.

The effects of the slit width are considered in Figure 6(b) when the period is 400 nm and the thickness is 800 nm. Although the field distribution in Figure 5 mainly shows node and anti-node formations in the vertical direction, the resonance condition can be affected by the lateral size of the cavity as well. In fact, the x components of the wavevector of diffracted waves are modified by the grating equation, resulting in nonzero values even at normal incidence. Hence, the standing wave formation in the lateral direction can occur with the presence of diffracted waves. Furthermore, boundary conditions at $z = 0$ and $z = d$ will also be modified as the lateral dimension of the cavity changes. Figure 6(b) clearly shows that the peak wavelengths shift to the shorter wavelength region when the slit width changes from 100 nm to 300 nm. Interestingly, even for the narrow slit when the aspect ratio w/d is 0.125, the cavity resonance still enhances the transmission through the slit array, allowing the transmittance to be over 0.85. When $w = 300$ nm, the overall transmittance is already very high, such that the cavity resonance does not considerably enhance the transmission. The number of peaks does not change as the slit width changes. Again, the transmittance peak due to Wood's anomaly does not shift in Figures 6(a and b) since the grating period remains the same.

Figure 6(c) shows the transmittance of gratings when the grating period is either 400 nm, 600 nm, or 800 nm while $d = 800$ nm and $w = 200$ nm. Unlike the previous structures, the physical size of individual cavity remains the same, and only the lateral size of metal strips changes. Since the grating period changes, the wavelength corresponding to Wood's anomaly accordingly shifts as seen from Figure 6(c). The effects of the grating period on the resonance condition are very similar to those of the slit width, such that the transmittance peak wavelength shifts to longer wavelengths as the period increases. As mentioned earlier, standing waves in the lateral direction formed by diffracted waves also contributes to the resonance condition. In terms of the standing wave formation in the x direction, increases in w or k_{xj} (i.e., decreases in Λ) while keeping the other constant have the same effects because the phase shift in the cavity of each diffracted wave is proportional to the product of $k_{xj}w$. Hence, Figures 6(b and c) show very similar trends in the transmittance peak wavelengths as w increases or as Λ decreases. Furthermore, the transmittance peak around $\lambda = 600$ nm becomes broader when $\Lambda = 800$ nm. In this case, additional propagating orders $j = \pm 1$ exist based on Eq. (3a) because the wavelength 600 nm is shorter than the period. In Figures 6(a and b), however, only the zeroth-order diffracted wave is propagating when the cavity resonance occurs. The existence of the additional propagating diffraction orders may affect the far-field transmission characteristics, such that the transmittance at cavity resonance becomes broader.

The transmittance of the Ag grating with the same geometric parameters as in Figure 3 is plotted with respect

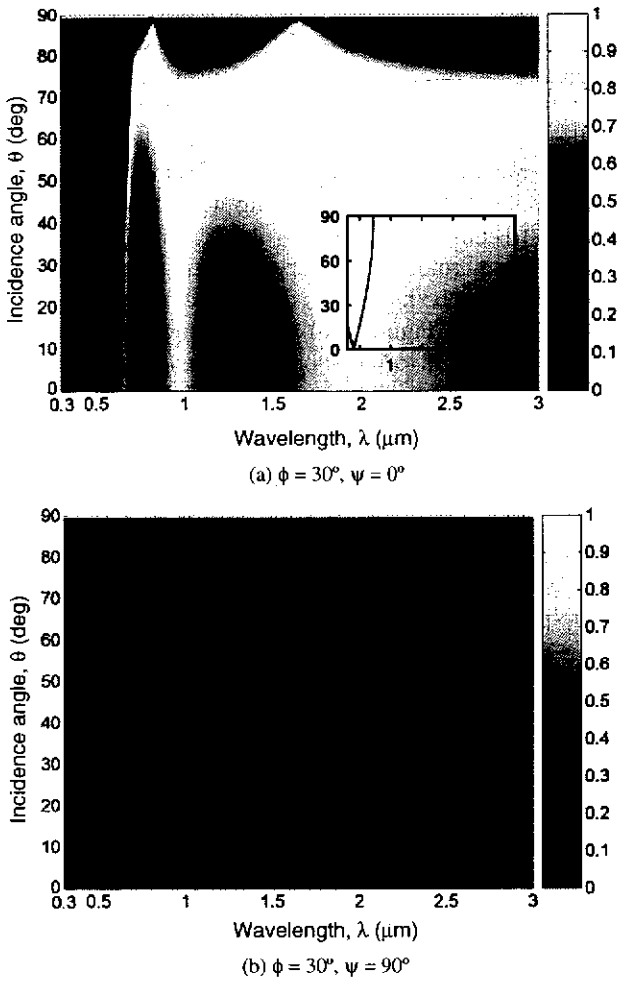

Fig. 7. Contour plot of the transmittance with respect to the wavelength and the incidence angle for the grating with the same geometric parameters as in Figure 3: (a) $\phi = 30°$ and $\psi = 0°$; (b) $\phi = 30°$ and $\psi = 90°$. The inset shows the solution of Wood's anomaly determined by Eq. (13).

to the wavelength and incidence angle for $\phi = 30°$, i.e., conical diffraction, in Figure 7 for TM ($\psi = 0°$) and TE ($\psi = 90°$) waves, respectively. The inset in Figure 7(a) depicts the solutions of Wood's anomaly obtained from Eq. (13) with a minor (short) branch ($j = 1$) on the lower-left corner and a major (long) branch ($j = -1$) that across all zenith angles. Because the excitation of SPP is at wavelengths very close to Wood's anomaly, a reduction of the transmittance due to enhanced absorptance can be seen in the major branch and especially for TM waves. On the other hand, the minor branch of Wood's anomaly may enhance the transmittance for TE waves, as can be seen from the bright region at the lower-left corner of Figure 7(b). As can be seen from Figure 7(a), oscillations of the transmittance due to the cavity resonance are obvious along the wavelengths for different θ values less than 45°, and the transmittance peak positions are close to those in Figure 3(b) for $\phi = 0°$. On the other hand, for $60° < \theta < 70°$, the spectral transmittance is greater than 0.8 at wavelengths longer than 1 μm, without visible oscillations. Even when $\theta > 80°$, there exists considerable transmission through the Ag grating with $T \approx 0.6$ at the wavelengths of 875 and 1750 nm. As can be seen from Figure 7(b), the transmittance for TE waves exhibits quite different features with much lower values compared with those for TM waves. As shown in Figures 3 and 4, the cutoff wavelength of cavity resonance for TE wave is around 500 nm at normal incidence. When $\phi = 30°$, the transmittance values are much higher than those in Figure 3(a) because H_y is not zero.

3.3. Effective Medium

A mixture of multiple media or a complicated structure can be homogenized into an effective medium with a specific material property to reduce the computational time with reasonably approximate results.[15] For 1D gratings, the EMT is applicable only when all diffraction orders are evanescent except the zeroth order.[21] Since the grating period in the present work is much shorter than the wavelength in the mid-IR spectral region, the grating (Region II) can be modeled by a homogeneous film of thickness d. The zeroth-order effective medium expression has been used for the design of periodic gratings with antireflection effects[30] or wavelength-selective radiative properties.[31] On the other hand, expressions containing high-order terms of Λ/λ often failed for metallic gratings, resulting in negative values in the imaginary part of the effective dielectric function.[21] Therefore, the zeroth-order expression is adopted in the present study, and the dielectric functions are given below for both polarizations when the PoI is perpendicular to the grating grooves:

$$\varepsilon_{TE} = f\varepsilon_A + (1-f)\varepsilon_B \tag{14a}$$

and

$$\varepsilon_{TM} = \left(\frac{f}{\varepsilon_A} + \frac{1-f}{\varepsilon_B}\right)^{-1} \tag{14b}$$

where f is the filling ratio of medium A, which is Ag in the present study. It is important to note that the dielectric functions depend on the polarization of the incident wave so that the effective medium behaves differently for different polarizations. Furthermore, the grating filling ratio is the only geometric parameter affecting the dielectric function.

Figure 8(a) shows the effective refractive index and extinction coefficient for the TM wave when the filling ratio of the Ag grating is 0.5. The effective extinction coefficient becomes three orders smaller than that of Ag and thus behaves like a dielectric material. On the contrary, the effective extinction coefficient for the TE wave (not shown in the figure) has the same order of magnitude as that of bulk Ag. Consequently, grating behaves like a metal film for the TE wave so that most radiation is reflected. Figure 8(b) shows the transmittance spectra calculated by EMT for Ag gratings with a thickness $d = 800$ nm and filling ratio $f = 0.5$. Note that the result

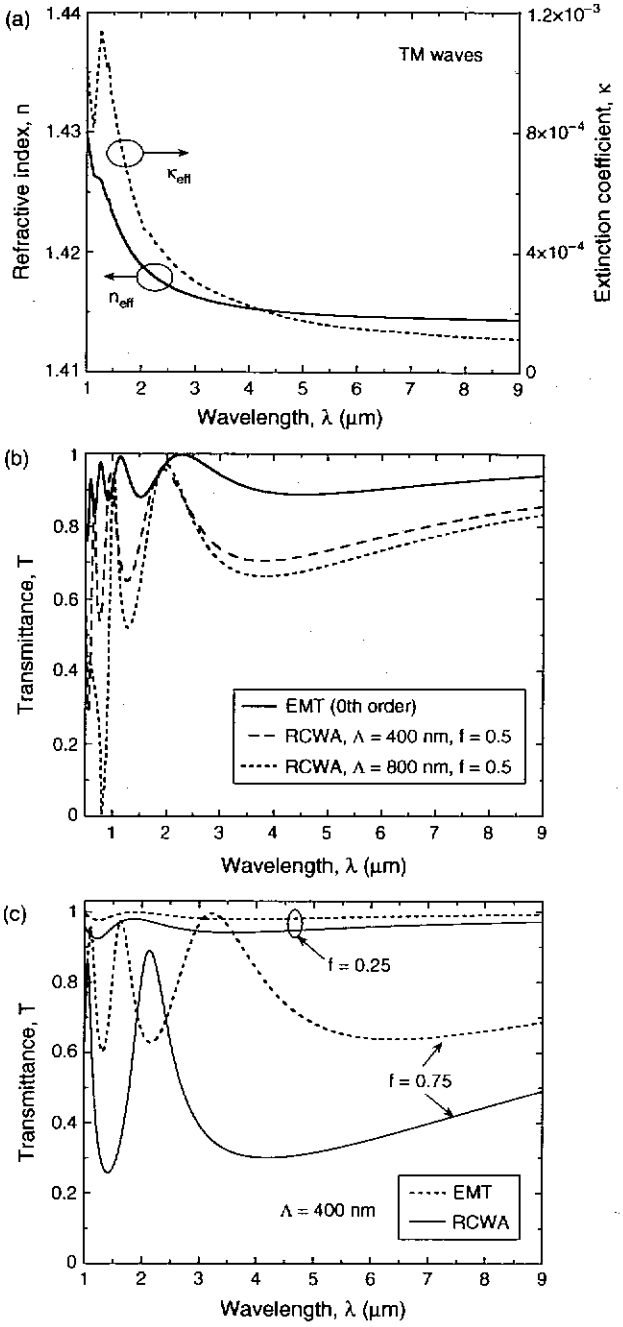

Fig. 8. Effective medium behavior of the grating structure in the mid-IR spectral region for the TM wave: (a) effective optical constants of the Ag grating with $f = 0.5$; (b) transmittance based on the EMT (solid line) when $\Lambda = 400$ nm, $d = 800$ nm, and $f = 0.5$, and those from RCWA for gratings (dashed line for $\Lambda = 400$ nm; dash-dotted line for $\Lambda = 800$ nm) with the same f and d; (c) transmittance from the EMT (dotted lines) and RCWA (solid lines) with different filling ratios when $\Lambda = 400$ nm and $d = 800$ nm.

from EMT (solid line) is independent of the grating period. The transmittance spectra, calculated by RCWA, of two Ag gratings (i.e., $\Lambda = 400$ nm; dashed line and $\Lambda = 800$ nm; dash-dotted line) with the same filling ratio and the thickness are also plotted for comparison. The trend of transmittance predicted from EMT agrees well with those calculated from RCWA, especially at long wavelengths. On the other hand, the deviation becomes large at short wavelengths especially for $\Lambda = 800$ nm. While EMT predicts oscillations due to thin-film interference, it fails to describe the cavity resonance of the gratings in the near-infrared region. The effect of filling ratio on the TM wave transmittance of the Ag slit array is examined with $\Lambda = 400$ nm and $d = 800$ nm with $f = 0.25$ and 0.75, as shown in Figure 8(c). Though the transmittance by the EMT shows a similar trend as that by RCWA for different filling ratios, the deviation becomes larger as the filling ratio increases. In general, EMT overpredicts the transmittance and the error becomes larger as the filling ratio increases. For the TE wave, the transmittance is very close to zero in the mid-IR region when the filling ratio is greater than 0.05.

The effects of θ are further investigated in the long wavelength region with the same geometric parameters as

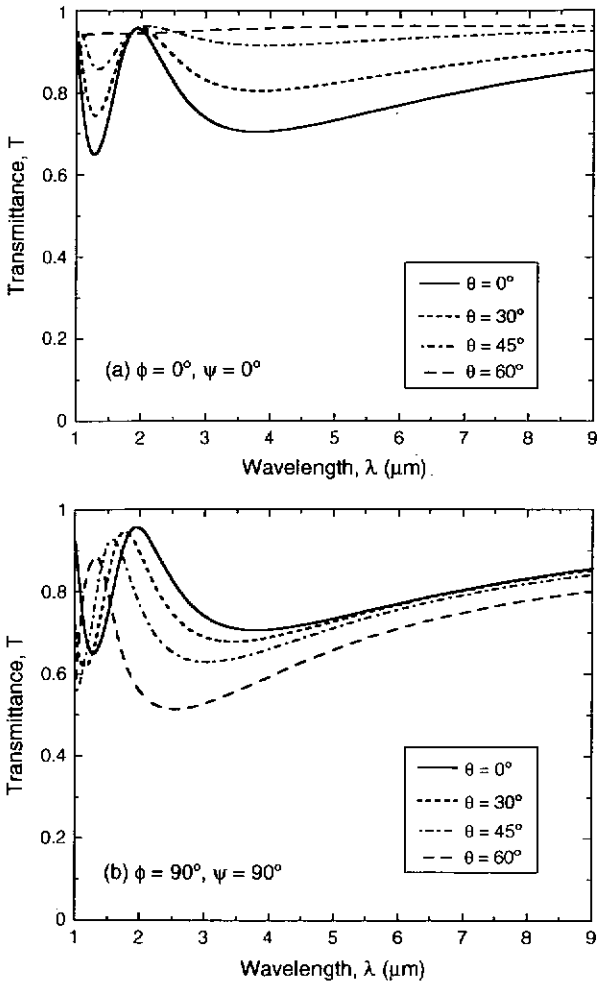

Fig. 9. Transmittance of the Ag grating with the same geometric parameters as in Figure 3: (a) the plane of incidence is perpendicular to the grating grooves; (b) the plane of incidence is parallel to the grating grooves. In both cases, the magnetic field is set to be parallel to the grating grooves.

those in Figure 3 using RCWA. Figure 9 plots the transmittance spectra of the free-standing grating when the PoI is either perpendicular or parallel to the grating grooves. Note that the transmittance spectra for $\theta = 0°$ are identical in Figures 9(a and b). In Figure 9(a), with $\phi = 0°$ and $\psi = 0°$, the magnetic field is always parallel to the grooves. Furthermore, k_x increases with θ but k_y remains zero. As θ increases, the transmittance increases in the mid-IR. Similar variations in the transmittance can also be predicted by EMT based on the TM wave, although it is not shown here. The transmittance at large incidence angles ($\theta \geq 60°$) is close to unity in the whole spectrum. It appears that the transmittance peak due the cavity resonance at $\lambda \approx 2.0$ μm is independent of θ when $\theta \leq 45°$. Notice that only E_x and E_z change as θ varies but H_y remains the same, suggesting that the y-component of the magnetic field plays a dominant role in the cavity resonance for TM waves. On the other hand, if H_y changes, the wavelength corresponding to the cavity resonance varies somewhat as shown in Figure 9(b), and the spectral transmittance decreases as θ increases. Although Figure 9(b) is for TE incidence with $\phi = 90°$ and $\psi = 90°$, the electric field is always perpendicular to the grooves. Furthermore, $k_x = 0$ and k_y increases with θ. The situation corresponds to conical diffraction. The magnetic field has a component H_y that is parallel to the grooves. Hence, the transmittance is relatively large in the mid-IR but decreases with increasing θ. This is caused by the reduction of the ratio H_y/H_z as θ increases. Therefore, the dependence of transmittance on θ has opposite trends in Figures 9(a and b). In the case of Figure 9(b), the EMT formula is not applicable because of conical diffraction. When there is a nonzero electric field component E_y, e.g., $\phi = 90°$ and $\psi = 0°$, the transmittance becomes very small in the long wavelength region.

Figure 10 shows the magnetic field distribution at $\lambda = 8$ μm when the TM wave is incident on the same structure considered in Figure 3. At $\lambda = 8$ μm, the wavelength-to-period and wavelength-to-slit ratios are 20 and 40, respectively. When the grating exhibits an effective medium behavior, the magnetic field in the vicinity of grating does not contain rich features like those of Wood's anomaly and the cavity resonance. Instead, the magnetic-field intensity is nearly uniform around the grating, except the Ag strips where it decays very fast. Figure 10 also arrows the time-averaged Poynting vector, defined as $\mathbf{S} = 0.5\mathrm{Re}[\mathbf{E} \times \mathbf{H}^*]$, where Re represents the real part of complex quantity. The arrows represent the directions of the Poynting vector and indicate the path of net energy flow. The magnitude of Poynting vector in vacuum of the grating region is greater than that of Regions I and III, as illustrated by the longer arrows, because energy transferred through Ag strips is negligible. Therefore, the incident energy is squeezed into the narrow slit regions. The Poynting vector distribution quickly evens out within a distance around 200 nm from the grating surface. Note that the Poynting vectors become the largest around the sharp corners of the slits; this may be caused by the abrupt change of material properties at the corner. The figure is a clear illustration of how the IR radiation can be funneled through the nanometer scale grating structures. More detailed discussion about the near-field localization of the IR radiation in the nanometer length scale through the 1D metallic gratings can be found in the Ref. [16].

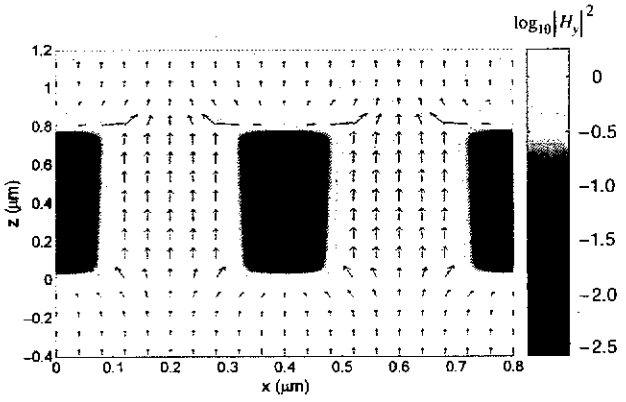

Fig. 10. Square of the magnitude of complex magnetic field and Poynting vector distribution for TM waves over the two grating periods at $\lambda = 8$ μm. The field is plotted as a contour plot, and the Poynting vector is illustrated in arrows. The geometric parameters of the Ag grating are the same as in Figure 3. The slit regions are located in the regions 0.1 μm $\leq x \leq 0.3$ μm and 0.5 μm $\leq x \leq 0.7$ μm.

4. CONCLUSIONS

In the present study, the transmission enhancement in the spectral region from visible to mid-infrared through nanoscale 1D slit arrays has been theoretically examined, using a modified RCWA algorithm, based on both the far-field spectral transmittance and the field distributions near the grating region. The mechanisms enabling large transmission are Wood's anomaly, cavity resonance, and the effective medium behavior, depending on the spectral region. For TE waves, spectral transmittance shows peaks due to Wood's anomaly and the cavity resonance in the visible region with transmittance peaks partly overlapped. On the other hand, the influence of Wood's anomaly and the cavity resonance are separated for TM waves. Near the wavelength corresponding to Wood's anomaly, the field distribution in the vicinity of the grating can be strongly affected by the interference of diffracted evanescent waves and propagating waves. Hence, Wood's anomaly can also suppress the transmittance, along with the excitation of SPPs. The cavity resonance yields transmittance oscillation in both TE and TM waves, with very large transmittance maxima for TM waves at the resonance wavelengths. The resonance wavelengths depend strongly on the polarization and can also be affected by the thickness, period, and the slit width of gratings. This is because all diffracted waves are responsible in forming standing waves inside the cavity. In the mid-IR spectral region, however, the effective

medium theory can explain the large transmission found in a wavelength-insensitive manner for TM waves, as well as the nearly-zero transmittance for TE waves. Based on the EMT, the grating structure behaves like a metal for the TE wave but a dielectric for the TM wave. The Poynting vector distribution in the near-field regime clearly shows that the incident radiation can be efficiently funneled through the narrow slit region even when $w{:}\lambda = 1{:}40$.

Acknowledgment: This work was supported by the National Science Foundation (CTS-0500113).

References

1. T. W. Ebbesen, H. J. Lezec, H. F. Ghaemi, T. Thio, and P. A. Wolff, *Nature* 391, 667 (**1998**).
2. E. Popov, M. Nevière, S. Enoch, and R. Reinisch, *Phys. Rev. B* 62, 16100 (**2000**).
3. H. J. Lezec and T. Thio, *Opt. Express* 12, 3629 (**2004**).
4. W. Srituravanich, N. Fang, C. Sun, Q. Luo, and X. Zhang, *Nano Lett.* 4, 1085 (**2004**).
5. F. J. García-Vidal and L. Martín-Moreno, *Phys. Rev. B* 66, 155412 (**2002**).
6. J. A. Porto, F. J. García-Vidal, and J. B. Pendry, *Phys. Rev. Lett.* 83, 2845 (**1999**).
7. M. Auslender and S. Hava, *Infrared Phys. Technol.* 36, 1077 (**1995**).
8. S. Astilean, Ph. Lalanne, and M. Palamaru, *Opt. Commun.* 175, 265 (**2000**).
9. F. Marquier, J.-J. Greffet, S. Collin, F. Pardo, and J. L. Pelouard, *Opt. Express* 13, 70 (**2005**).
10. R. W. Wood, *Phys. Rev.* 48, 928 (**1935**).
11. A. Hessel and A. A. Oliner, *Appl. Opt.* 4, 1275 (**1965**).
12. H. Raether, Surface Plasmons on Smooth and Rough Surfaces and on Gratings, Springer-Verlag, Berlin (**1988**).
13. J.-J. Greffet, R. Carminati, K. Joulain, J.-P. Mulet, S. Mainguy, and Y. Chen, *Nature* 416, 61 (**2002**).
14. F. Marquier, M. Laroche, R. Carminati, and J.-J. Greffet, *J. Heat Transfer* 129, 11 (**2007**).
15. P. Lalanne and D. Lemercier-Lalanne, *J. Mod. Opt.* 43, 2063 (**1996**).
16. B. J. Lee, Y.-B. Chen, and Z. M. Zhang, *J. Quant. Spectroc. Radiat. Transfer* 109, 608 (**2008**).
17. M. G. Moharam, E. B. Grann, D. A. Pommet, and T. K. Gaylord, *J. Opt. Soc. Am. A* 12, 1068 (**1995**).
18. L. F. Li, *J. Opt. Soc. Am. A* 13, 1870 (**1996**).
19. S. T. Han, Y. L. Tsao, R. M. Walser, and M. F. Becker, *Appl. Opt.* 31, 2343 (**1992**).
20. S. Peng and G. M. Morris, *J. Opt. Soc. Am. A* 12, 1087 (**1995**).
21. Y.-B. Chen, Z. M. Zhang, and P. J. Timans, *J. Heat Transfer* 129, 79 (**2007**).
22. P. Lalanne and G. Morris, *J. Opt. Soc. Am. A* 13, 779 (**1996**).
23. E. D. Palik, Handbook of Optical Constants of Solids, Vol. 1, Academic Press, San Diego, CA (**1998**).
24. Y.-B. Chen and Z. M. Zhang, *Opt. Commun.* 269, 411 (**2007**).
25. H. F. Ghaemi, T. Thio, D. E. Grupp, T. W. Ebbesen, and H. J. Lezec, *Phys. Rev. B* 58, 6779 (**1998**).
26. A. K. Azad, Y. Zhao, and W. Zhang, *Appl. Phys. Lett.* 86, 141102 (**2005**).
27. M. Born and E. Wolf, Principles of Optics, 7th edn., Cambridge University Press, Cambridge, UK (**1999**).
28. S. Maruyama, T. Kashiwa, H. Yugami, and M. Esashi, *Appl. Phys. Lett.* 79, 1393 (**2001**).
29. H. Sai, Y. Kanamori, K. Hane, and H. Yugami, *J. Opt. Soc. Am. A* 22, 1805 (**2005**).
30. A. Sentenac and J.-J. Greffet, *Int. J. Heat Mass Transfer* 37, 553 (**1994**).
31. E. N. Glytsis and T. K. Gaylord, *Appl. Opt.* 31, 4459 (**1992**).

Received: 5 August 2006. Accepted: 30 January 2007.